Effects of Disks on Gravitational Lensing by Spiral Galaxies

Share Your Story

EFFECTS OF DISKS ON GRAVITATIONAL LENSING BY SPIRAL GALAXIES

MATTHIAS BARTELMANN

Max-Planck-Institut für Astrophysik, P.O. Box 1523, D-85740 Garching, Germany

AND

ABRAHAM LOEB

Harvard-Smithsonian Center for Astrophysics, 60 Garden Street, Cambridge, MA 02138

ABSTRACT

Gravitational lensing of a quasar by a spiral galaxy should often be accompanied by damped Lyα absorption and dust extinction due to the intervening gaseous disk. In nearly edge-on configurations, the surface mass density of the gas and stars in the disk could by itself split the quasar image and contribute significantly to the overall lensing cross section. We calculate the lensing probability of a disk-plus-halo mass model for spiral galaxies, including the cosmic evolution of the lens parameters. A considerable fraction of the lens systems produce two images with subarcsecond separation, straddling a nearly edge-on disk. Because of that, extinction by dust together with observational selection effects (involving a minimum separation and a maximum flux ratio for the lensed images) suppress the detection efficiency of spiral lenses in optical wave bands by at least an order of magnitude. The missing lenses could be recovered in radio surveys. In modifying the statistics of damped Lyα absorbers, the effect of extinction dominates over the magnification bias due to lensing.

Subject headings: cosmology: theory — galaxies: spiral — gravitational lensing — quasars: absorption lines

1. INTRODUCTION

Gravitational lensing by a spiral galaxy occurs when the line of sight to a background quasar passes within a few kiloparsecs from the center of the galactic disk. Since galactic disks are rich in neutral hydrogen (H I), the quasar spectrum is likely to show a damped Lyα absorption trough at the lens redshift. Therefore, the efficiency of blind searches for gravitational lensing with subarcsecond splitting can be enhanced by more than an order of magnitude by selecting a subset of all bright quasars that show a low-redshift ($z \lesssim 1$) damped Lyα absorption with a high H I column density, $\gtrsim 10^{21}$ cm^{-2} (Bartelmann & Loeb 1996). Moreover, multiply imaged quasars could be identified spectroscopically through their multiple-trough absorption spectra. The composite spectrum of a lensed quasar is a superposition of the spectra received from the different images that intersect the absorbing disk at different locations, probe different H I column densities, and hence acquire different widths in their damped Lyα troughs (Loeb 1997).

The magnification bias due to lensing changes the statistics of damped Lyα absorbers (DLAs) in quasar spectra by bringing into view quasars that would otherwise fall below the detection threshold (Bartelmann & Loeb 1996; Smette, Claeskens, & Surdej 1997). For optical observations, this effect is counteracted by dust extinction in the lensing galaxy (Malhotra, Rhoads, & Turner 1997; Perna, Loeb, & Bartelmann 1997). The combination of lensing and dust extinction results in a net distortion of the H I column density distribution of DLAs.

Since galactic disks are thin, their own surface mass density could exceed the critical value necessary for image splitting when they happen to be projected nearly edge-on. In such orientations, a pair of quasar images will straddle the symmetry axis of the disk rather than its center. When averaged over all possible disk orientations, the total lensing cross section of the disk-plus-halo mass distribution should still be roughly the same as that of a halo with the same spherically averaged mass profile (Wang & Turner 1997; Keeton & Kochanek 1998). However, when lensing by the disk is included in the calculation, the effects of dust extinction and H I absorption are substantially different because of the new predominant image configurations straddling edge-on disks.

Previous theoretical studies have either ignored the possibility of lensing by the disk itself (Bartelmann & Loeb 1996; Smette et al. 1997) or else ignored the effects of dust extinction or H I absorption on the lensing statistics (Maller, Flores, & Primack 1997; Wang & Turner 1997; Keeton & Kochanek 1998). In addition, these discussions did not examine the implications of evolution in the spiral lens population for its overall lensing properties and statistics. In this paper, we include all of the above ingredients. Our model evolves the number density of galaxies based on the Press-Schechter (1974) theory for dark matter halos, combined with simple evolutionary scaling laws for the disk properties inside these halos (Mo, Mao, & White 1997).

In § 2 we describe our model for the mass and H I distributions in galactic disks, as well as our model for their dust content. We also summarize the adopted scaling laws for the evolution of the lens population with redshift. In § 3 we compute the lensing cross sections, imaging probabilities, and lensing statistics of our model spiral galaxies. The impact of dust on the lensing statistics and the effect of lensing on the statistics of DLAs are examined in § 4. Finally, § 5 summarizes the main conclusions from this work.

2. A LENS MODEL FOR SPIRAL GALAXIES

2.1. *Mass Model and Lensing Properties*

We use a mass model for spiral lenses that was recently suggested by Keeton & Kochanek (1998). The model consists of oblate, ellipsoidal, isothermal building blocks for

individual mass components. They have the axisymmetric density distribution

$$\rho(R, z) = \frac{v_c^2}{4\pi G q_3} \frac{e}{\sin^{-1} e} \frac{1}{R^2 + s^2 + x_3^2/q_3^2} , \quad (1)$$

where R is the distance from the symmetry axis of the ellipsoid, x_3 is the distance from its midplane, q_3 is the axis ratio, s is the core radius which softens the mass distribution, v_c is the asymptotic circular velocity, and e is the eccentricity of the mass distribution,

$$e = (1 - q_3^2)^{1/2} . \quad (2)$$

Hence, each mass component is described by one parameter quantifying its dynamical properties, namely, the circular velocity v_c, and two parameters characterizing its shape, namely, the core radius s and the oblateness q_3.

The projection of the three-dimensional density ρ results in the two-dimensional surface mass density

$$\Sigma(x) = \frac{\Sigma_{cr}}{2} b_p [q^2(s^2 + x_1^2) + x_2^2]^{-1/2} . \quad (3)$$

Here Σ_{cr} is the critical surface mass density for lensing,

$$\Sigma_{cr} = \frac{c^2}{4\pi G} \frac{D_s}{D_l D_{ls}} , \quad (4)$$

where D_l, D_s, and D_{ls} are the angular-diameter distances between the observer and the lens, the observer and the source, and the lens and the source, respectively. The angular position vector on the sky is $x = (x_1, x_2)$, and

$$b_p = 2\pi \left(\frac{v_c}{c}\right)^2 \frac{D_l D_{ls}}{D_s} \frac{e}{\sin^{-1} e} = b \frac{e}{\sin^{-1} e} , \quad (5)$$

where b is the Einstein radius of a singular isothermal sphere with a circular velocity v_c. Finally, q is the projected axis ratio

$$q = (q_3^2 \sin^2 i + \cos^2 i)^{1/2} , \quad (6)$$

where i is the inclination angle of the disk relative to the line of sight, with $i = 0$ for a face-on orientation.

As shown by Keeton & Kochanek (1998), the lensing potential of the surface-mass density (3) is

$$\psi(s, q_3) = x_1 \alpha_1 + x_2 \alpha_2 - b_p s$$
$$\times \ln [(\varrho + s)^2 + (1 - q^2)x_1^2]^{1/2} , \quad (7)$$

with

$$\varrho = [q^2(x_1^2 + s^2) + x_2^2]^{1/2} ,$$
$$\alpha_1 = \frac{b_p}{(1 - q^2)^{1/2}} \tan^{-1} \left[\frac{(1 - q^2)^{1/2} x_1}{\varrho + s}\right],$$
$$\alpha_2 = \frac{b_p}{(1 - q^2)^{1/2}} \tanh^{-1} \left[\frac{(1 - q^2)^{1/2} x_2}{\varrho + q^2 s}\right]. \quad (8)$$

We now combine three of the isothermal oblate ellipsoids to a mass model consisting of a *maximal* disk and a surrounding halo. The total lensing potential then reads

$$\psi = \psi(s_d, q_{3d}) - \psi(r_d, q_{3d}) + \psi(s_h, 1) , \quad (9)$$

where $s_{d,h}$ are the core radii of disk and halo, respectively, q_{3d} is the disk axis ratio, and r_d is the disk truncation radius,
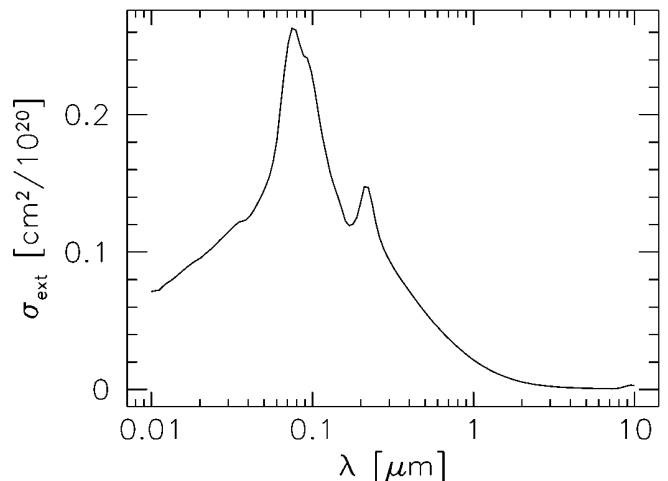

Fig. 1.—Rotation curve of a model consisting of a truncated Mestel disk embedded in an isothermal halo, with $v_c = 220$ km s^{-1}. The curve steeply rises to v_c and then levels off, being flat to better than 5% at large radii.

or disk radius for simplicity. The first term is the potential of a disk with an asymptotically flat rotation curve, axis ratio q_{3d}, and core radius s_d. The second term truncates that disk at radius r_d. The third term adds the surrounding spherical halo necessary to maintain a flat rotation curve beyond the disk truncation radius. This is the maximal *truncated Mestel disk*[1] model introduced by Keeton & Kochanek (1998). All lensing properties of the combined model can now be calculated in terms of the potential ψ.

To completely define the model, we need to specify five parameters, namely, the circular velocity v_c, the two core radii $s_{d,h}$, the disk radius r_d, and the disk oblateness q_{3d}. For reference, we define $v_{c*} = 220$ km s^{-1}, $r_{d*} = 8 h^{-1}$ kpc, and $q_{3d*} = 0.03$. Requiring a flat rotation curve, we must then use $s_{h*} \approx 0.72 r_{d*}$ (Keeton & Kochanek 1998). Finally, we choose $s_{d*} = 0.2 h^{-1}$ kpc. The rotation curve of this model is plotted in Figure 1. As the figure shows, the rotation curve is flat to better than 5% beyond a radius of $\sim 2 h^{-1}$ kpc.

To illustrate the lensing properties of the combined disk-plus-halo model described by equation (9), we show in Figure 2 the caustics and critical curve configuration for a disk inclination angle of $i = 80°$. The lens has two critical curves and caustics. The inner caustic, which is the image of the outer critical curve, has the familiar astroid shape with four cusps connected by folds.

2.2. *Neutral Hydrogen Disk*

Next, we address the effects of the gaseous component of the disk. To evaluate the level of dust extinction and H I absorption, we assume that the H I density, n_H, follows a double-exponential profile,

$$n_H(R, x_3) = n_{H,0} \exp\left(-\frac{|x_3|}{H}\right) \exp\left(-\frac{R}{R_0}\right). \quad (10)$$

The three parameters that define this profile are the central neutral hydrogen density $n_{H,0}$, the disk scale height H, and the disk scale length R_0. In order to keep the

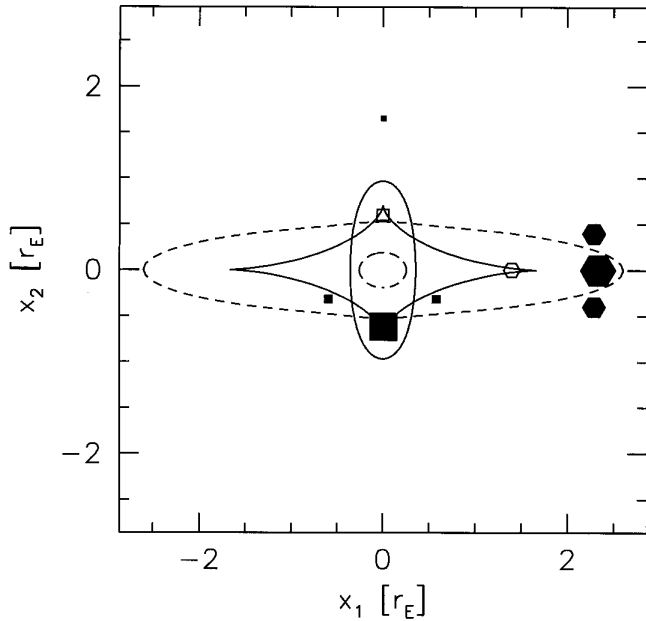[1] For $s_d \to 0$, the disk becomes a Mestel (1963) disk.

FIG. 2.—Critical curves (*dashed lines*) and caustics (*solid lines*) for a disk-plus-halo lens. Since nearly edge-on configurations are preferred both geometrically and by the magnification bias, we show results for a disk inclination angle of $i = 80°$. The caustic corresponding to the outer critical curve shows the familiar astroid shape with four cusps connected by folds. The substantial contribution of the disk to the surface mass density stretches the caustic along the symmetry axis of the projected disk. For illustration, we plot image configurations (*filled squares and hexagons*) for two source positions (*empty square and hexagon*). Sources in the region surrounded by two caustics have five images, one of which is located close to the center and highly demagnified. Sources between the inner and the outer caustic have three images.

number of free parameters small in our model, we assume $H = q_3 r_d$ and $R_0 = r_d$, so that the H I scale height is given by the short axis of the oblate ellipsoid used to describe the lensing disk. We also identify the H I scale radius with the truncation radius for the lensing disk. The radial shape of the resulting radial H I profile is similar to that observed in local disk galaxies (Broeils & van Woerden 1994). We choose $n_{H,0}$ so that the face-on H I column density, $N_0 = 2Hn_{H,0}$, corresponds to the characteristic observed value (Broeils & van Woerden 1994), $N_0 \approx 11.25 \times 10^{20}$ cm^{-2}. Hereafter, we use the notation $N = 10^{20}N_{20}$ cm^{-2}. Note that with these parameter choices, the solar neighborhood values for the H I column density ($N_{HI} = 7.4 \times 10^{20}$ cm^{-2}; Kulkarni & Heiles 1987) and H I scale height (a few hundred pc; Knapp 1987) of the Milky Way disk are reproduced reasonably well. Changing the disk scale height up or down by a factor of 2 does not significantly alter the results.

We ignore the consumption of H I gas by star formation. A complete model for the evolution of H I in spiral galaxies should include various feedback effects of stars on the disks in which they form, such as heating, ionization, or expulsion of gas by supernova-driven winds. For the purposes of this study, we prefer to avoid the highly uncertain nature of these effects and focus on a simple model.

2.3. Extinction by Dust

We assume for simplicity that the distribution of dust follows equation (10) with a constant ratio of dust to H I gas. This implies dust scale heights that are somewhat larger than typically observed (e.g., Kylafis & Bahcall 1987), but

there are counterexamples (Xilouris et al. 1997) with larger dust scale height.

We adopt the scattering and absorption cross sections due to silicates and graphites derived by Draine & Lee (1984). The total extinction cross section is the sum of the contributions from scattering and absorption, and the relative proportion of these components is chosen so as to fit best the observed Galactic extinction law. Figure 3 shows the sum σ_{ext} of the extinction cross sections from graphites and silicates as a function of wavelength, assuming a dust-to-gas ratio of 1:100 by mass (Whittet 1992).

The dust optical depth is given by

$$\tau_{ext}(\lambda) = N\sigma_{ext}(\lambda) , \qquad (11)$$

so that the extinction in magnitudes is

$$\Delta m(\lambda) = |\, 2.5 \log_{10} \{\exp\left[-\,N\sigma_{ext}(\lambda)\right]\} \,| \approx 1.09 N\sigma_{ext}(\lambda) . \qquad (12)$$

In quantifying the influence of dust, we restrict our attention to the *observer's* Johnson B band. In the rest frame of a lens at a redshift z_l, this band is centered on the wavelength $\lambda_l = 0.435\ \mu$m $(1 + z_l)^{-1}$. For $z_l = 0.3$, Figure 3 yields $\sigma_{ext} N \approx 0.084 N_{20}$. Hence, for $N = 10^{21}$ cm^{-2}, $\Delta m \approx 0.9$ magnitudes in the B band. Note that N can easily exceed this value for edge-on disks, which are favored both geometrically and due to the magnification bias. The value of N can be as large as $N_0 R/H = N_0/q_3 \approx 3.4 \times 10^{22}$ cm^{-2}, yielding $\Delta m \approx 31$ for a lens at $z_l = 0.3$. This implies that the influence of dust on the imaging properties of spiral lenses can be severe.

One would expect the dust-to-gas ratio of spiral disks to decline with increasing redshift, in accordance with their metallicity history. Indeed, Pei, Fall, & Bechtold (1991) infer that the dust-to-gas ratio in DLAs at redshifts $2 \lesssim z \lesssim 3$ is only a tenth of the Milky Way value, although with considerable scatter (Fall & Pei 1993). If we parameterize the dust content to have a power-law dependence on redshift, $(1 + z)^{-\delta}$, then a reduction by a factor of ~ 10 from the present time to $z \approx 2.3$ implies $\delta \approx 2$. Equation (12) is then
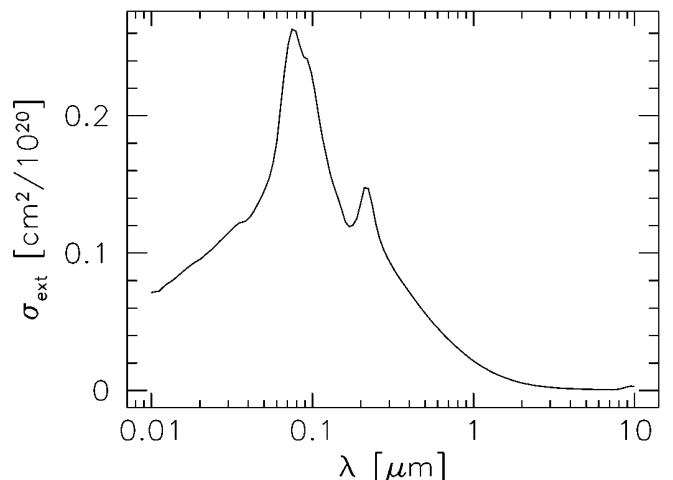

FIG. 3.—Sum of the extinction cross sections for scattering and absorption by graphites and silicates. The total cross section, $\sigma_{ext}(\lambda)$, is given in units of cm^2 per 10^{20} hydrogen atoms, assuming a gas-to-dust fraction of 1:100 by mass, following Draine & Lee (1984).

changed to

$$\Delta m(\lambda, z_l) \approx 1.09(1 + z_l)^{-2} N_{20} \, \sigma_{\rm ext}\left(\frac{\lambda}{1 + z_l}\right). \quad (13)$$

This dependence will be referred to as the *dust evolution model* in the discussion that follows. Strictly speaking, we should adapt our model to reproduce the observed optical depth of dust rather than the dust-to-gas ratio, but since our model well reproduces the observed H I column density distribution (see Fig. 10 and Tytler 1987; Lanzetta et al. 1991), we can safely calibrate the dust content in the way described.

2.4. Scalings of Galaxy Properties with Luminosity

We assume that the lens population admits the Schechter luminosity function at present with a number density per unit luminosity,

$$\frac{dn(l)}{dl} \, dl = n_* \, l^\nu \, \exp\,(-l) dl \,, \quad (14)$$

where $l \equiv L/L_*$ is the scaled galaxy luminosity. For spiral galaxies, $n_* = 1.5 \times 10^{-2} \, h^3 \, {\rm Mpc}^{-3}$ and $\nu = -0.81$ (Marzke et al. 1994). The luminosity is related to the circular velocity through the Tully-Fisher (1977) relation,

$$\frac{v_c}{v_{c*}} = l^{1/\alpha} \,, \quad (15)$$

where α varies between ~ 2 in the B band and ~ 4 in the H band (see review by Strauss & Willick 1995, and references therein).

Equations (5) and (15) imply that the Einstein radius scales as $b \propto l^{2/\alpha}$. The computational effort required later on is substantially reduced if the scale radii of the disk-plus-halo model change with l in the same way as b does. For convenience, we therefore adopt the infrared value of $\alpha = 4$ and assume that the scale radii behave like $r_d \propto l^{1/2}$.[2] It is then sufficient to calculate all cross sections for one reference luminosity only and later scale the result to the desired l by changing the Einstein radius. If σ_* is the cross section for some arbitrary image properties for the reference luminosity L_*, then the average cross section for the entire population of spiral galaxies is

$$\langle\sigma\rangle = n_* \int_0^\infty dl\sigma_* \, l^{4/\alpha}l^\nu \, \exp\,(-l)$$

$$= n_* \, \Gamma(1 + \nu + 4/\alpha)\sigma_* \,. \quad (16)$$

2.5. Evolution of the Spiral Galaxy Population

The simplest assumption about the evolution of the spiral population is that they maintain a constant comoving number density, $n(z) = n(0)(1 + z)^3$, and constant scale radii. This is the *no-evolution* model. Alternatively, Mo et al. (1997) recently suggested a model for the evolution of spirals, based on four assumptions: (1) the disk mass is a fixed fraction m_d of the halo mass; (2) the disk angular momentum is a fixed fraction j_d of the halo's angular momentum; (3) the radial disk profile is exponential, and the disk is centrifugally supported; and (4) the disk is dynamically stable. These assumptions yield a set of simple and straightforward scaling relations, which we reproduce from Mo et al. (1997; see also Fall & Efstathiou 1980).

We assume that the halo is a singular isothermal sphere with a radial density profile,

$$\rho = \frac{v_c^2}{4\pi G r^2} \,. \quad (17)$$

Taking the virial radius r_{200} as the size of the halo, the halo mass is $M = v_c^2 \, r_{200}/G$. Here r_{200} is the radius within which the average halo density is 200 times the *critical* density of the universe,

$$\frac{3M}{4\pi r_{200}^3} = 200 \times \frac{3H^2(z)}{8\pi G} \,, \quad (18)$$

and hence

$$r_{200}(z) = \frac{v_c}{10H(z)} \approx 220 \, h^{-1} \, {\rm kpc} \left(\frac{v_c}{220 \,{\rm km\,s}^{-1}}\right)\left[\frac{H(z)}{H_0}\right]^{-1} \,,$$
$$(19)$$

where $H_0 = 100 \, h \, {\rm km\,s}^{-1} \, {\rm Mpc}^{-1}$ is the Hubble constant, and $H(z)$ is the Hubble parameter at redshift z. Similarly,

$$M(z) = \frac{v_c^3}{10GH(z)} \approx 2.5 \times 10^{12} \, h^{-1} \, M_\odot$$

$$\times \left(\frac{v_c}{220 \,{\rm km\,s}^{-1}}\right)^3\left[\frac{H(z)}{H_0}\right]^{-1} \,. \quad (20)$$

The disk radius r_d is related to the spin parameter of the halo, $\lambda \; (\equiv J \, |E|^{1/2}/GM^{5/2}$, where J and E are the total angular momentum and energy of the halo, respectively), by

$$r_d = \frac{\lambda v_c}{10\sqrt{2}H(z)}\left(\frac{j_d}{m_d}\right) \approx 7.8 \, h^{-1} \, {\rm kpc} \left(\frac{\lambda}{0.05}\right)$$

$$\times \left(\frac{v_c}{220}\right)\left(\frac{j_d}{m_d}\right)\left[\frac{H(z)}{H_0}\right]^{-1} \,, \quad (21)$$

and the central surface mass density of the disk is[3]

$$\Sigma_0 = \frac{10}{\pi} \frac{m_d v_c H(z)}{G\lambda^2}\left(\frac{m_d}{j_d}\right)^2$$

$$\approx 6.8 \times 10^{-2} \, h \, {\rm g\,cm}^{-2} \left(\frac{m_d}{0.05}\right)\left(\frac{\lambda}{0.05}\right)^{-2}$$

$$\times \left(\frac{v_c}{220 \,{\rm km\,s}^{-1}}\right)\left(\frac{m_d}{j_d}\right)^2\left[\frac{H(z)}{H_0}\right] \,. \quad (22)$$

---

[2] Since $r_d \propto l^{1/2}$ implies constant surface brightness, the chosen scaling reflects Freeman's law (Freeman 1970; Holmberg 1975; Peterson, Strom, & Strom 1979; van der Kruit 1987; Lauberts & Valentijn 1989). Thus, we effectively ignore the scatter in Freeman's law and the influence of low surface brightness (LSB) galaxies on the lensing cross section (e.g., Bothun, Impey, & McGaugh 1997 and references therein). This omission is justified here because (1) the average circular velocities of LSB galaxies is somewhat lower than that of high–surface brightness (HSB) galaxies, and the lensing cross section is a sensitive function of the circular velocity, and (2) LSB galaxies are less compact than HSB galaxies and thus less efficient lenses. For the purposes of strong lensing, it therefore seems safe to neglect any contribution from LSB galaxies.

[3] Different realizations of galaxy formation in different tidal environments could result in disks of different sizes for the same halo properties, due to variations in the spin parameter acquired by the baryons. As discussed before, we ignore this scatter in the disk properties here.

In summary, scale radii scales as $v_c H(z)^{-1}$, and the surface mass density[4] scales as $v_c H(z)$. Since the characteristic values of λ, j_d, and m_d are expected to depend very weakly on redshift, we use these simple proportionality relations with v_c and $H(z)$ in scaling the properties of the local spiral population to higher redshifts. Since $H(z)/H_0 > 1$ for $z > 0$, scale radii *decrease* with increasing z, while the surface mass density *increases* with increasing z.

The evolution in the number density of spiral galaxies can be expressed in terms of the Press-Schechter distribution function for the mass M, given by equation (20). We evolve the number density of galaxies given by equations (14), (15), and (20) with the factor $n_{PS}(M, z)/n_{PS}(M, z = 0)$, where $n_{PS}(M, z)$ is the Press-Schechter number density of halos with mass M at redshift z. Because of the inherent uncertainty in modeling galaxy evolution, we present numerical results for three models, assuming (1) no evolution, (2) evolution of scale radii only, and (3) evolution of galaxy number density and scale radii.

It is well known that the present-day Press-Schechter mass function extends out to halo masses that are well beyond the galactic mass scale (e.g., Navarro, Frenk, & White 1995) in all viable models of structure formation. This is because of the fact that the nonlinear mass scale at present (which defines the exponential break in the Press-Schechter mass function) corresponds to a much larger circular velocity than L_* in the Schechter function does, based on the Tully-Fisher relation (see eqs. [14] and [15]). This implies that nongravitational processes (such as inefficient cooling or expulsion of gas by supernovae) prevented disk formation inside supergalactic halos at the present time. An evolutionary model for galaxies based solely on the Press-Schechter approach is therefore incomplete. The simplest interpretation of the discrepancy between the Press-Schechter mass function and the local luminosity function of galaxies is that massive galaxies with $L \gtrsim L_*$ have not changed their dynamical properties since the redshift of galaxy formation ($z \sim 2$–4) when the nonlinear mass scale was comparable to their mass. Indeed, recent observations imply no significant evolution in the population of massive galaxies out to redshifts $z \sim 1$ (Ellis 1997 and references therein; but see Kauffmann, Charlot, & White 1996). However, the same observations reveal many more dwarf galaxies at high redshift than are found locally. Since the lensing probability is dominated by L_* galaxies at $z \lesssim 0.7$, the no-evolution model might be more appropriate for calculations of lensing by disk galaxies. However, to bracket the other extreme of complete evolution we also show results for the Press-Schechter prediction. Since we use the Press-Schechter mass function only to correct the overall normalization of the number density of spiral galaxies relative to its present-day value, our approach should be less affected by the incompleteness of the Press-Schechter treatment.

In all numerical calculations, we use the cosmological parameters $\Omega_0 = 0.3$, $\Omega_\Lambda = 0$, and $h = 0.7$. For the Press-Schechter mass function, we use the standard CDM power spectrum (Bardeen et al. 1986) with the normalization $\sigma_{8h^{-1}Mpc} = 1$. A cosmological model with these parameters

reproduces the local abundance of rich galaxy clusters (White, Efstathiou, & Frenk 1993; Eke, Cole, & Frenk 1996; Viana & Liddle 1996), has the shape parameter $\Omega_0 h = 0.21$ preferred by analyses of galaxy clustering (Peacock & Dodds 1994), but has a somewhat higher normalization than that derived from the *COBE* data (e.g., Ratra et al. 1997). It also agrees with the observed abundance of giant luminous arcs in galaxy clusters (Bartelmann et al. 1998).

3. LENSING CROSS SECTIONS

Next, we proceed to calculate the magnification cross section of the disk-plus-halo lenses. This calculation must be done numerically. First, we cover the source plane with a grid of source positions. Far from the lens center, the resolution of this grid can be low, while close to the caustic curves where the highest magnifications arise, the resolution should be high. We therefore use an adaptive grid in the source plane whose resolution increases toward the caustic curves. Then, for each source position, all image positions need to be found. For this purpose, we use the algorithm described by Schneider, Ehlers, & Falco (1992). Briefly, it is based on covering the image plane with a uniform grid, which is then mapped back to the source plane. All grid cells on the image plane whose mapping on the source plane contains the source position are taken to contain images of the source. In regions of strong lensing, the parity of the cell might be flipped when it is mapped into the source plane; i.e., corners of the cell might be interchanged. One should therefore start with triangular rather than rectangular cells in the image plane, because the image of a triangle remains a convex figure whose interior is well defined. This can be easily achieved by splitting each rectangular cell along one of its diagonals. Here again, we use an adaptive-grid approach in order to achieve high resolution at a reasonable computational cost. First, the image positions are searched on a coarse grid, constraining the regions on the lens plane where the images are located. Then each of these regions is covered with a fine grid on which the final image positions are localized. This way, all the images corresponding to every segment on the source-plane grid are identified.

The magnification of each image can then be computed from the total lensing potential (eq. [9]),

$$\mu_{GL} = \det^{-1}\left(\delta_{jk} - \frac{\partial^2 \psi}{\partial x_j \partial x_k}\right), \qquad (23)$$

evaluated at each of the image positions x_i. When dust extinction is included, the effective magnification of an image at position x_i is

$$\mu(x_i) = \mu_{GL}(x_i) \exp\left[-N(x_i)\sigma_{ext}\right], \qquad (24)$$

where $N(x_i)$ is the H I column density at the position of the image. The net magnification is the sum of the moduli of the effective magnifications for all of its N images,

$$\mu = \sum_{i=1}^{N} |\mu(x_i)|. \qquad (25)$$

This approach yields maps of the source magnification in the source plane. The magnification cross sections can be extracted from these maps as the area in the source plane within which sources are magnified by a factor $\geq \mu$. The magnification cross section depends on the orientation of the disk relative to the line of sight. Denoting the cross section for a magnification $\geq \mu$ and a disk inclination angle
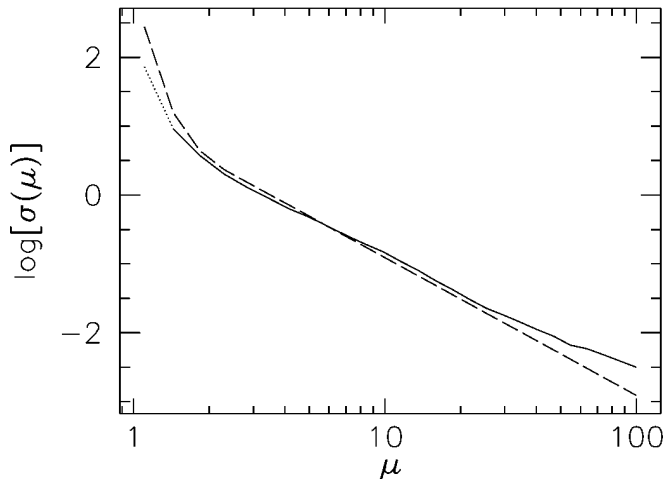
FIG. 4.—Inclination-averaged magnification cross section of a disk-plus-halo lens (*solid line*) compared to that of a singular isothermal sphere (*dashed line*) with the same circular velocity. The source redshift is $z_s = 2$, and the lens redshift is $z_l = 0.3$. The cross sections are given in units of the Einstein disk area, πb^2. At small magnifications ($\mu \sim 1$) the cross section of the spiral lens becomes difficult to evaluate numerically, as indicated by the dotted section of the solid curve. The cross sections are almost identical, except for high magnifications, where the disk-plus-halo model has a slightly larger cross section than the singular isothermal sphere.

i by $\sigma'(\mu, i)$, we obtain the inclination-averaged cross section through the integral,

$$\sigma(\mu) = \int_0^{\pi/2} di \, \sin \, (i)\sigma'(\mu, i) \, . \qquad (26)$$

Obviously, $\sigma(\mu)$ depends on the cosmological distances involved and on the other lens parameters. We suppress these dependences here for brevity.

Figure 4 shows that the inclination-averaged magnification cross section of the disk-plus-halo model is almost identical to that of a singular isothermal sphere with the same circular velocity. Without imposing further conditions, such as a minimum image separation or a maximum
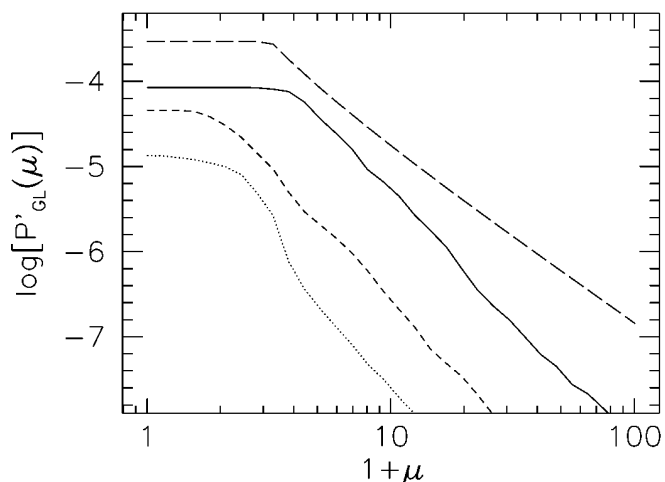

FIG. 5.—Probability $P'_{GL}(\mu)$ for a quasar at a redshift $z_s = 2$ to be multiply imaged with magnification $> \mu$, image separation $> 0\overset{''}{.}3$, and flux ratio of the images < 20. The curves are for the disk-plus-halo model without dust (*solid line*), with nonevolving dust (*dotted line*), and with evolving dust (*short-dashed line*). We compare these results to a mass model of a singular isothermal sphere with no dust and the same asymptotic circular velocity as the disk-plus-halo model (*long-dashed line*). These curves do not include evolution of scale lengths or number density of the lens population. Here and in all the following figures, results for the singular isothermal sphere model are calculated without dust extinction.

flux ratio between the images, the lensing statistics of spiral lenses is well described by the simple spherical halo model. We will demonstrate below what happens when further constraints are imposed on the image properties.

In the limit of small magnifications ($\mu \to 1$), the cross section for the disk-plus-halo model becomes numerically incomplete; this follows from the fact that the cross section increases rapidly as $\mu \to 1$, while the simulation is spatially bounded. This limit is irrelevant for our purposes, because we always impose further imaging constraints. In particular, when we require the image separation and flux ratio to be bounded to reasonable limits, the cross section is confined to the multiple-imaging region, which is entirely contained within our simulated section of the source plane.

3.1. *Imaging Probabilities*

Given the inclination-averaged cross sections, the probability for a (point) source at redshift z_s to be imaged with magnification $\geq \mu$ is obtained by the line-of-sight integral over the density of lenses times their lensing cross section, $\sigma(\mu)$. For the model without number-density evolution, this integral yields

$$P'_{GL}(\mu) = n_* b_*^2 \, \Gamma\left(1 + v + \frac{4}{\alpha}\right) \int_0^{z_s} dz(1 + z)^3$$

$$\times \left(\frac{D_{ls}}{D_s}\right)^2 \left|\frac{c \, dt}{dz}\right| \sigma(\mu) \, , \qquad (27)$$

where $|c \, dt/dz|$ is the proper-distance interval corresponding to the redshift interval dz. The factor $n_* b_*^2 \, \Gamma(1 + v + 4/\alpha)$ comes from integrating over the luminosity distribution of the spiral galaxies (see eq. [16]). When evolution of the galaxy population is taken into account as described in § 2.5, the factor $(1 + z)^3$ above is changed to $n_{PS}(M_*, z)/n_{PS}(M_*, 0)(1 + z)^3$, where $M_*(z)$ is the mass of a galaxy with circular velocity v_{c*} at the corresponding redshift.

Now let $|dN_{QSO}/dS|(S)dS$ be the intrinsic number density of quasars at redshift z_s with a flux between S and $S + dS$. Accounting for magnification bias, the number of lensed quasars is

$$N'_{QSO}(S) = \int_0^\infty dS' P'_{GL}\left(\frac{S}{S'}\right) \frac{dN_{QSO}}{dS}(S') \, , \qquad (28)$$

and hence the probability for a quasar at redshift z_s to be detected with flux $> S$ is

$$P_{GL}(S) = \frac{1}{N_{QSO}(S)} \int_0^\infty dS' P'_{GL}\left(\frac{S}{S'}\right) \frac{dN_{QSO}}{dS}(S') \, . \qquad (29)$$

We approximate the observed quasar number counts in the B band by a broken power law,

$$\frac{dN_{QSO}}{dS} = \begin{cases} (S/S_0)^a & \text{for } S \leq S_0 \, , \\ (S/S_0)^b & \text{for } S > S_0 \, , \end{cases} \qquad (30)$$

where S_0 corresponds to $B_{QSO} \approx 19$. For quasar redshifts $z_s \sim 2$, $a = -1.64$ and $b = -3.52$ (e.g., Pei 1995).

Figure 5 shows $P'_{GL}(\mu)$, and Figure 6 shows $P_{GL}(S)$ for the no-evolution galaxy model. These figures include curves that illustrate the influence of nonevolving and evolving dust. All curves in Figure 5 were calculated under the additional constraints that the two brightest images be separated by $\geq 0\overset{''}{.}3$ and that their flux ratio be ≤ 20. The solid and long-dashed curves in Figure 5 are for the disk-plus-halo
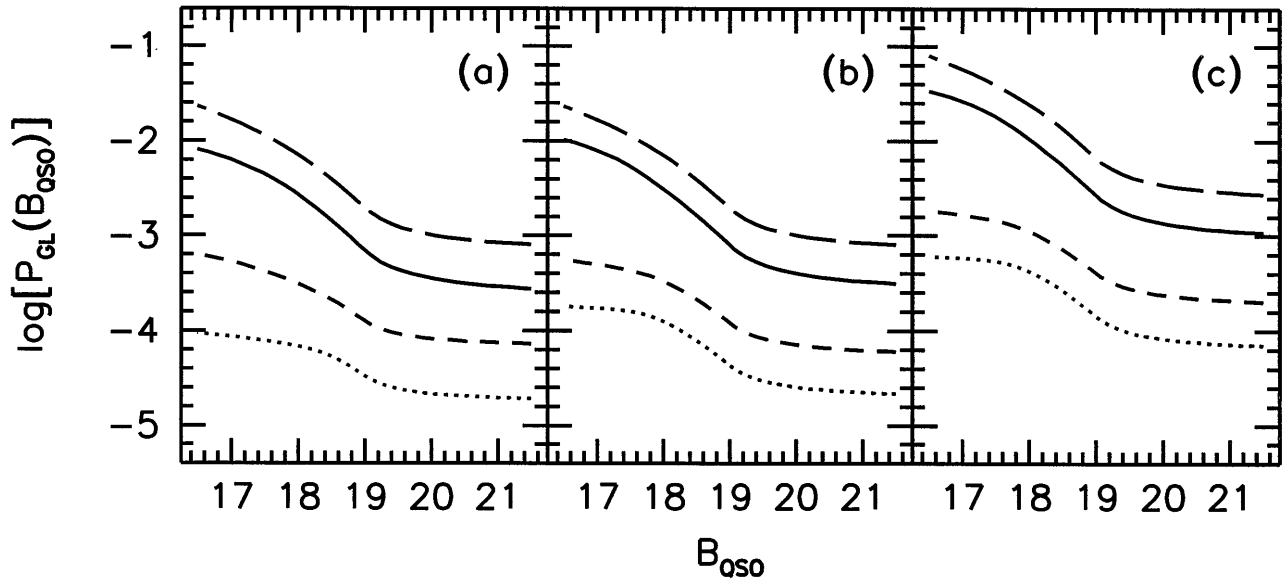
FIG. 6.—Probability $P_{GL}(B_{QSO})$ for a quasar to be multiply imaged with image separation $> 0\overset{''}{.}3$ and flux ratio < 20, as a function of B_{QSO}. The mass model includes (a) no evolution, (b) evolution of disk scale lengths, and (c) evolution of scale lengths and number density. The four curves per panel are for the disk model without dust (*solid curve*), with nonevolving dust (*dotted curve*), and with evolving dust (*short-dashed curve*), and the singular isothermal sphere model (*long-dashed curve*).

model and for the singular isothermal sphere, respectively. Evidently, the disk-plus-halo model is less efficient at producing multiple images with the specified properties than the singular isothermal sphere, despite the fact that the total magnification cross sections of the two models are close to each other (Fig. 4). The reason for this difference is that the images produced by the spiral lens model are typically closer to each other than those of the singular isothermal sphere and are occasionally below the $0\overset{''}{.}3$ threshold. This occurs because a significant fraction of the lensing cross section is contributed by the disk in nearly edge-on orientations. The image separation on either side of the disk is then smaller than the Einstein diameter of the corresponding singular isothermal sphere.

The imposed constraints on the minimum image separation and maximum flux ratio approximately reflect characteristic thresholds for detecting a multiply imaged system through space-based observations with finite resolution and dynamical range (see Kochanek 1993). Figure 5 demonstrates that these additional constraints reduce the detection efficiency of spiral lenses considerably compared to the singular isothermal sphere model. The figure also quantifies the severe effect that dust extinction has on the detection efficiency. Besides suppressing the detection probability by 1 or 2 orders of magnitude for evolving and nonevolving dust, respectively, the dust extinction allows for values of $\mu = (S_{observed}/S_{intrinsic})$ smaller than unity, which are otherwise unphysical.

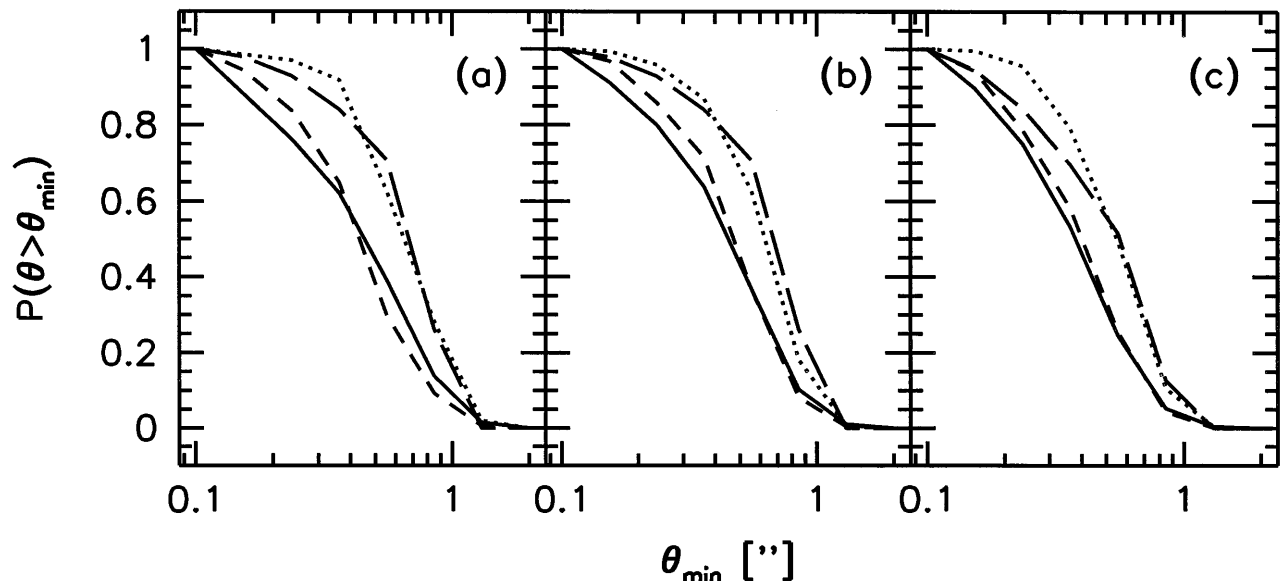FIG. 7.—Cumulative distribution of multiple images with separation $\theta > \theta_{min}$, as a function of θ_{min}, for a constant maximum flux ratio $r_{max} = 20$ and quasar magnitude $B_{QSO} = 18$. The disk model includes (a) no evolution, (b) evolution of scale lengths, and (c) evolution of scale lengths and disk number density. The three curves per panel are without dust extinction (*solid line*) and with extinction by nonevolving (*dotted*) and evolving (*short-dashed*) dust. The long-dashed curve describes the singular isothermal sphere model with no dust.
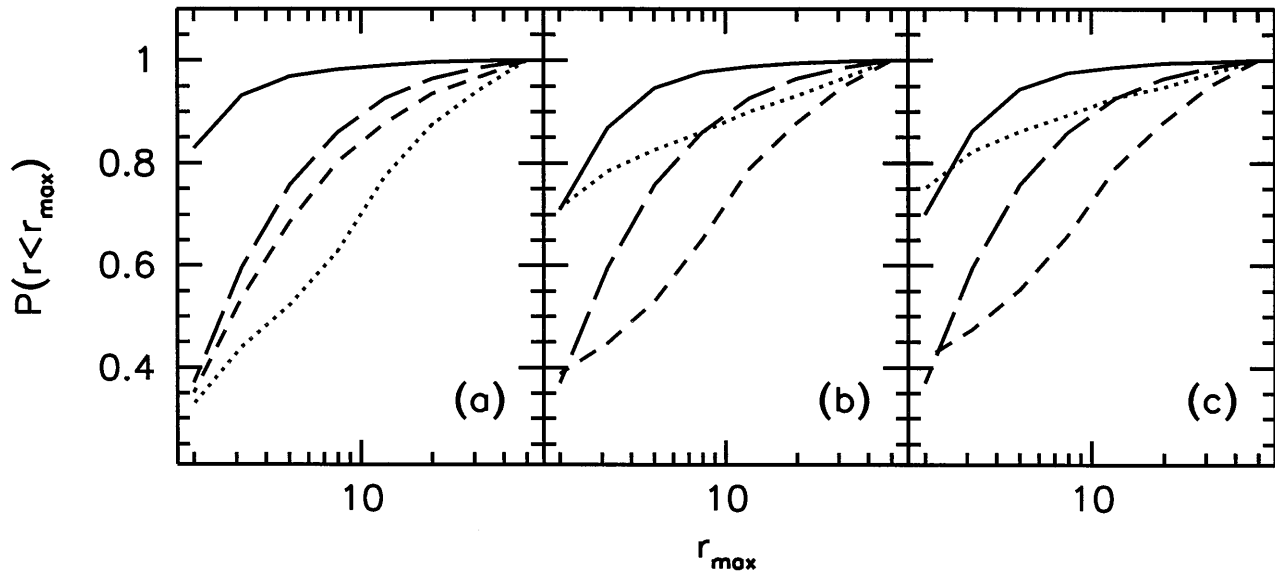
FIG. 8.—Cumulative distribution of multiple images with a B band flux ratio $r < r_{max}$, as a function of r_{max}, for a constant $\theta_{min} = 0\rlap{.}''3$ and $B_{QSO} = 18$. The panels and the curves have the same meaning as in the previous figure.

Figure 6 then shows the probability $P_{GL}(S)$ for quasars at redshift $z_s = 2$ to be lensed with image separation $\geq 0\rlap{.}''3$ and flux ratio ≤ 20 as a function of the quasar B magnitude. Again, the dotted and short-dashed curves are calculated including dust extinction, and the solid and long-dashed curves are without dust for the disk-plus-halo model and for the singular isothermal sphere model, respectively. The three panels in the figure are for different levels of cosmological evolution as detailed in the figure caption. The figure shows that bright quasars, with $B_{QSO} \leq 19$, are much more likely to be multiply imaged than faint quasars, because of the magnification bias. At $B_{QSO} \sim 18$, the multiple-imaging probability is about a factor of 5 higher than for $B_{QSO} \sim 19$. As already shown in Figure 5, dust extinction severely reduces the imaging probability, and it also leads to a

weaker rise in the lens detection probability with increasing quasar brightness.

3.2. Image Statistics

In order to appreciate the significance of the selection effects in identifying spiral lenses, it is instructive to examine the distribution of image separations and flux ratios. Figure 7 shows the cumulative distribution of multiple images as a function of the minimum image separation θ_{min}. The distribution is arbitrarily normalized to unity at $\theta_{min} = 0\rlap{.}''1$. As before, the three panels in the figure are for disks (a) with no evolution, (b) with evolution of scale radii only, and (c) with evolution of scale radii and galaxy number density. The three curves per panel are for models without dust (solid line), with nonevolving dust (dotted line), and with evolving
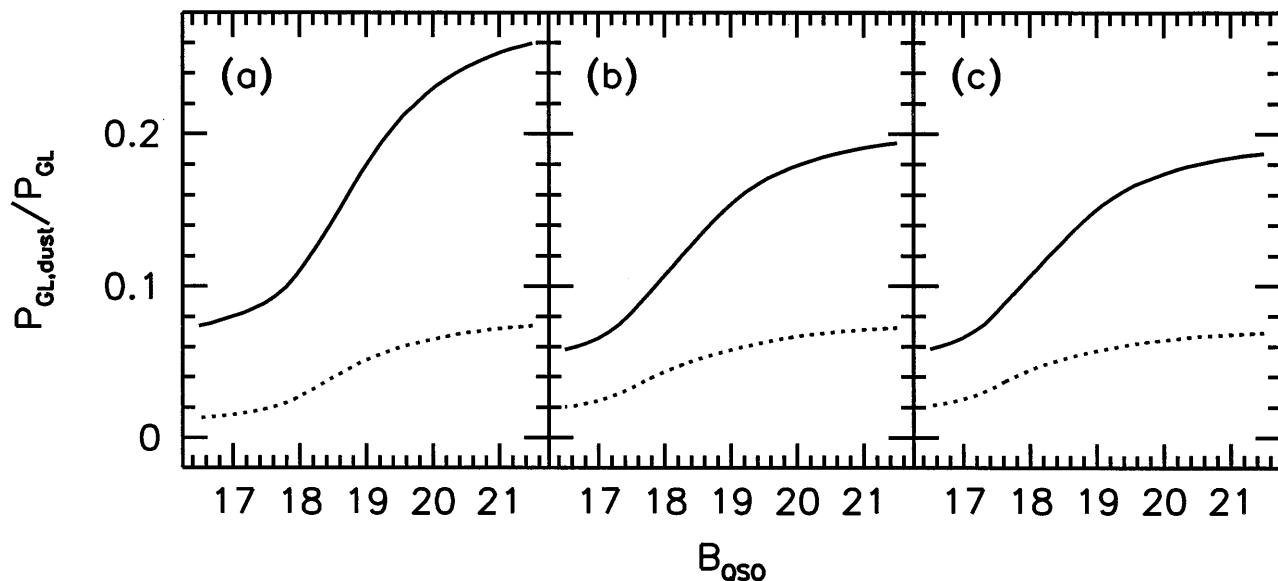

FIG. 9.—Reduction in the lens detection probability due to dust extinction in the (observer's) B band. We assume $\theta_{min} = 0\rlap{.}''3$ and $r_{max} = 20$. The curves show the lensing probability including dust divided by the lensing probability without dust, as functions of the quasars' B magnitude. The disk model has (a) no evolution, (b) evolution of scale lengths, and evolution of scale lengths and (c) disk number density. The two curves per panel are for nonevolving (dotted line) and evolving (solid line) dust.

dust (*short-dashed line*). The long-dashed curve in each panel shows the singular isothermal sphere model without dust for comparison.

Figure 7 implies that the median image separation is larger for the singular isothermal sphere than for the disk-plus-halo model. Images produced by the spiral lens model are on average closer to each other by $\sim 0\overset{''}{.}2$ than expected from the singular isothermal sphere model. This is because multiple images in the dust-plus-halo model are predominantly produced by the disk rather than by the halo, with a preference for nearly edge-on disk orientations.

Dust increases the average image separation because images with small separations occur close to the disk, where their flux is heavily suppressed by extinction. Disk evolution reduces the average image separation slightly, because the disks get more compact with increasing redshift. Number-density evolution according to the Press-Schechter model increases the abundance of field spirals at redshifts $z \sim 1$–2 (since some of these galaxies have subsequently merged and disappeared by now) and reduces the image separation further because the lenses are, on average, farther away.

Figure 8 shows the cumulative distribution of images as a function of the maximum flux ratio r_{max}, arbitrarily normalized to unity at $r_{max} = 50$. The notation is the same as in Figure 7. Generally, the curves for the disk-plus-halo model without dust are the flattest, showing that the images are usually of comparable brightness. When dust is included, the average flux ratio increases because of the strong extinction gradient around the disk.

4. EFFECTS OF THE GASEOUS DISK

4.1. *Impact of Dust on Lensing Statistics*

To further examine the influence of dust on the detectability of lensed quasars, we show in Figure 9 the ratio between the lensing probability $P_{GL}(B_{QSO})$ with and without dust. The three panels are again for a galaxy model (*a*) with no evolution, (*b*) with length-scale evolution only, and (*c*)

with length-scale plus number-density evolution. The two curves in each panel are for nonevolving and evolving dust (*dotted and solid lines, respectively*).

Figure 9 shows that the majority of all quasars that are lensed by spirals are undetectable in the *B* band. The deficit caused by dust increases for brighter quasars as a result of the magnification bias. At $B_{QSO} \approx 18$, only about 10% of all lensed quasars are observable, quite independent of the degree of evolution that is included in the calculation. If dust does not evolve with redshift, the deficit of lensed quasars is more severe. For faint quasars, $B_{QSO} \gtrsim 20$, the reduction in the lens detection probability is least severe in the no-evolution model. This is mainly because when disk evolution is included, the surface density of the disk increases with *z*, leading to more extensive dust extinction than the no-evolution model predicts.

Figure 9 implies that the fraction of quasars lensed by spiral galaxies in radio surveys should be higher by about an order of magnitude relative to that found in optical surveys.

4.2. *Statistics of Damped Lyα Absorption*

Based on the neutral hydrogen column density at the position of each image, we can investigate the influence of lensing and dust on the statistics of damped Lyα absorption by spirals. Let $P_{GL}(S, N)$ be the probability of observing a quasar with a flux $\geq S$ that is imaged by the population of spirals and shows an H I column density $> N$ in its spectrum. When there is more than one image, we take N to be the H I column density in the brightest image, i.e., that which dominates the absorption trough. As shown by Bartelmann & Loeb (1996), the observed column density distribution of neutral hydrogen is then given by

$$f(N) = \frac{c}{H_0} \frac{1}{\Delta X} \left| \frac{\partial P_{GL}(S, N)}{\partial N} \right|, \qquad (31)$$

where ΔX is the absorption distance scanned by the DLAs in the survey (Bahcall & Peebles 1969). Examples for the distribution of $Nf(N)$ are plotted in Figure 10.
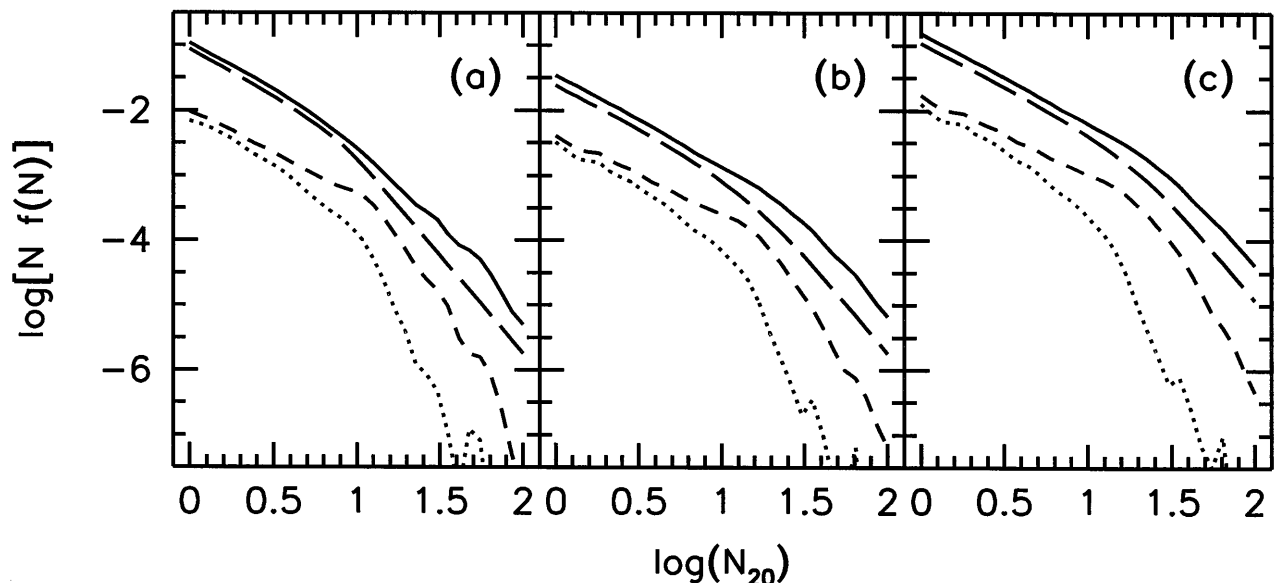

FIG. 10.—H I column-density distribution, $Nf(N)$, for lensed quasars with $B = 18$ at $z_s = 2$ as a function of $N_{20} \equiv (N/10^{20}\mathrm{cm}^{-2})$. The disk model includes (*a*) no evolution, (*b*) evolution of scale lengths, and evolution of scale lengths and (*c*) number density. The three curves were calculated without dust, with nonevolving dust, and with evolving dust (*solid, dotted, and short-dashed curves, respectively*). For reference, the long-dashed curve shows the result without lensing or dust extinction.

The inferred cosmological density parameter in neutral hydrogen, $\Omega_{\mathrm{H\,I}}$, traced by DLAs is given by

$$\Omega_{\mathrm{H\,I}} = \frac{H_0}{c} \frac{\bar{m}}{\rho_{\mathrm{cr,0}}} \int_{N_0}^{\infty} \mathrm{d}N N f(N) \,, \qquad (32)$$

where $\rho_{\mathrm{cr,0}}$ is the present-day critical density of the universe, $N_0 \approx 10^{20}$ cm^{-2} is the minimum column density for damped Lyα absorption, and $\bar{m}$ is the mean molecular mass. Because of the magnification bias, $f(N)$ depends on the quasar magnitude B_{QSO}, and so does the inferred $\Omega_{\mathrm{H\,I}}$. Figure 11 shows the ratio between the inferred and true values of $\Omega_{\mathrm{H\,I}}$ for spiral galaxies. The different panels and line types are the same as those in previous figures. Similarly to P_{GL}, $f(N)$ and $\Omega_{\mathrm{H\,I}}$ depend on the redshift range of the absorbers (see eq. [27]). We use the full redshift range, $0 \le z \le z_s = 2$, for Figure 10 and the upper panels of Figure 11, and the high-redshift range $1 \le z \le z_s$ for the lower panels of Figure 11.

Models without dust cause $\Omega_{\mathrm{H\,I}}$ to be overestimated by factors of up to a few in samples of bright quasars. The magnification bias brings into view quasars that were otherwise too faint to be detected. The lensed quasar images occur close to the lens center, where the H I column density is higher than average. However, when dust is included, the net effect is reversed. Now those quasars whose images are close to the disk are obscured, and the number of quasar spectra with high H I column density is lower. For evolving

dust and $B_{\mathrm{QSO}} \approx 18$, only about 20%–30% of the neutral hydrogen is detected.

At face value, the evolution model for spiral galaxies sketched in § 2.5 predicts decreasing $\Omega_{\mathrm{H\,I}}$ with increasing redshift. In contrast, for fixed source redshift, the observed $\Omega_{\mathrm{H\,I}}$ predicted by our model rises with absorber redshift, reaches a peak at intermediate redshifts, and falls toward the source redshift (see Fig. 3 in Bartelmann & Loeb 1996). This is a consequence of gravitational lensing, because the lensing efficiency is optimal when the lenses are located roughly halfway between observer and source. The *observed* change of $\Omega_{\mathrm{H\,I}}$ with redshift (e.g., Storrie-Lombardi, McMahon, & Irwin 1996) is thus qualitatively reproduced by our model, although the *intrinsic* $\Omega_{\mathrm{H\,I}}$ decreases with absorber redshift.

5. CONCLUSIONS

We investigated the lensing effects of spiral galaxies, modeled as maximal truncated Mestel disks embedded in spherical halos. This model makes the disk as massive as possible. Our results therefore represent the opposite extreme to the simple isothermal sphere models. Intermediate models with less massive disks would shift these results toward those obtained from the spherical model.

Although a disk-plus-halo configuration yields an inclination-averaged lensing cross section similar to that of the spherically symmetric mass distribution (Fig. 4), its
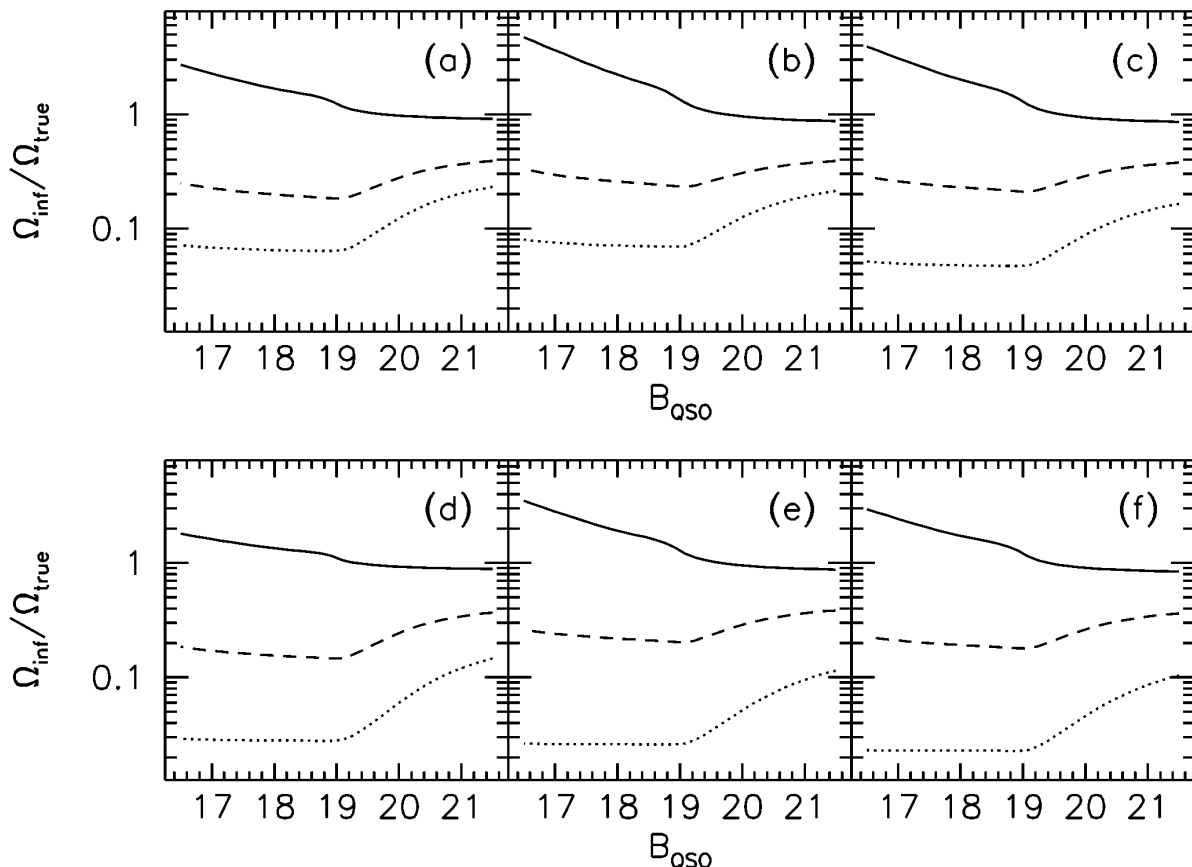

FIG. 11.—Ratio between the inferred and the true values of the density parameter of neutral hydrogen as a function of the quasar B magnitude. For the upper three panels, the redshift range for the absorbers is $0 \le z \le z_s = 2$, while for the lower panels it is restricted to $1 \le z \le z_s$. The disk model includes no evolution in panels (a) and (d), evolution of scale lengths in panels (b) and (e), and evolution of scale lengths and number density in panels (c) and (f). The three curves were calculated without dust, with nonevolving dust, and with evolving dust (solid, dotted, and dashed curves, respectively).

typical image separations are considerably smaller (Fig. 7). A substantial contribution to this cross section comes from lensing by nearly edge-on configurations of the disk, in which a pair of images straddles the disk. Because the images are often close to the disk, they suffer strong extinction by dust. The extinction lowers the detection efficiency of spiral lenses in the optical band by an order of magnitude. Moreover, disk lenses are often characterized by small image separation (Fig. 7) and large differential extinction (Fig. 8). As a result, the selection effects imposed by the finite angular resolution and dynamic range of observations set limits on the minimum image separation and their maximum flux ratio and substantially lower the probability for observing spiral lenses (see Fig. 9).

We find that dust dominates over the magnification bias because of lensing in modifying the statistics of damped Lyα absorption by spirals (Fig. 11). If most of the damped absorption systems are spirals, the inferred value of the cosmological density parameter in H I at $z \lesssim 1$ could be underestimated by a factor of a few.

The spiral-lens system B0218+357 shows compelling evidence for strong extinction. O'Dea et al. (1992) find that the quasar spectrum is red, Wiklind & Combes (1995) and Menten & Reid (1996) find strong molecular lines, and Grundahl & Hjorth (1995) find that image A is much fainter than image B in the optical in contrast to the radio observations, arguing for a substantial extinction of image A. Jaunsen & Hjorth (1997) have recently argued for the existence of disk lensing and associated extinction also in the lens system B1600+434, which has recently been modeled by Maller et al. (1997) and Koopmans, de Bruyn, & Jackson (1998). More generally, Malhotra et al. (1997) argue for a systematic reddening of lensed quasars relative to the rest of the quasar population, but they may have overestimated the effect (cf. Falco, Kochanek, & Muñoz 1998).

The optical depth to gravitational lensing of quasars was shown to be a very effective tool for setting constraints on the cosmological constant (Kochanek 1996 and references therein). In singular isothermal models, $\sim 80\%$–90% of the lensing probability is contributed by early-type galaxies (e.g., Fukugita & Turner 1991). However, if a significant fraction of the present-day early-type galaxies were in the form of spiral building blocks at $z \sim 1$ (as argued by Kauffmann et al. 1996), then the depletion of spiral lenses due to dust extinction and selection effects could weaken the current lensing constraints on the cosmological constant. This issue was addressed by Mao & Kochanek (1994) and Rix et al. (1994). They found that estimates of the cosmological constant from the statistics of strong lensing can be significantly changed only when the early-type galaxies seen today evolved dramatically below a redshift $z \sim 1$.

In this context, and in view of ongoing lensing surveys, it is instructive to examine which fraction of the total lensing optical depth is contributed by spirals rather than by early-type galaxies. To calculate this, we assume that the total galaxy population today is composed of 25% early-type galaxies and 75% spirals. We model spirals as described above and early-type galaxies as singular isothermal spheres with a characteristic velocity dispersion of $\sigma_{v*} = v_{c*}/2^{1/2} = 220$ km s^{-1}, following the Schechter luminosity function (14) and the Faber-Jackson (1976) relation. For simplicity, we use the same Schechter-function parameters as for the spirals. We consider two scenarios, one in which

the number density of early-type galaxies stays constant with redshift, and another in which early-type galaxies are assembled by merging of spirals. In the latter scenario, we assume that the number density of early-type galaxies changes with redshift as a power law, $n_E(z) = n_E(0)(1 + z)^\epsilon$, with $\epsilon \approx -1.6$, chosen such that $\sim \frac{2}{3}$ of the early-type galaxies are in the form of spiral building blocks at $z \sim 1$ (Kauffmann et al. 1996). We further assume that mergers conserve mass. In both scenarios, we can then compute the lensing optical depths for both spirals and early-type galaxies $P'_{\mathrm{GL};E,S}$ from equation (27) and the corresponding imaging probability $P_{\mathrm{GL};E,S}$ from equation (29) (under the constraints that the images be separated by $\geq 0\overset{''}{.}3$ and have a flux ratio ≤ 20).

Figure 12 shows the fraction of the total lensing probability contributed by spirals, namely $(P_{\mathrm{GL},S}/P_{\mathrm{GL,total}}) = P_{\mathrm{GL},S}/(P_{\mathrm{GL},E} + P_{\mathrm{GL},E})$. Figure 12a shows results for early-type galaxies with constant comoving number density, while Figure 12b examines the scenario in which early-type galaxies merge out of spirals. The three curves per panel are for spirals without dust, with nonevolving dust, and with evolving dust (solid, dotted, and dashed lines, respectively). The no-dust results are valid for radio-selected lenses. The solid line in panel (a) reproduces the familiar result that dust-free spirals contribute at most $\sim 20\%$ of the multiple-imaging probability, even for the small image-separation cutoff of $\theta_{\mathrm{min}} = 0\overset{''}{.}3$; this fraction is lower for higher θ_{min}. In the presence of dust, the fraction contributed by spirals is considerably smaller. In the merger scenario, the spiral lens fraction rises to $\sim 50\%$ without dust, $\sim 9\%$ with evolving dust, for quasars with $B \sim 18$. Thus, up to half of the lenses found in radio surveys (which are sensitive to small image separations) might be imaged by spirals.

Figure 9 implies that radio surveys should be about a factor of 5–10 more efficient at detecting spiral lenses than optical surveys. The recent CLASS and JVAS radio surveys indeed provide preliminary hints of a more substantial population of spiral lenses than found in optical surveys (cf. Table 1 in Browne et al. 1997; Jackson, Nair, & Browne 1997; but see Fassnacht & Cohen 1998). To date, the combined CLASS and JVAS samples encompass more than 10^4 flat-spectrum radio sources, 11 of which have been identified as lens systems. A substantial fraction of those have been classified as being lensed by spirals or S0 galaxies.[5] Because of their small image separation and simple geometry, lenses containing edge-on disks might offer a unique opportunity for estimating the masses of galactic disks at high redshifts and also for constraining the Hubble constant based on the time delay between the flux variations in their images. Indeed, the time delay in B0218 has been measured to 12 ± 3 days, translating to a Hubble constant of $H_0 \sim 60$ km s^{-1} Mpc^{-1} (Corbett et al. 1996), and B1608+656 offers another promising lens system for this purpose (Myers et al. 1995; Fassnacht et al. 1996).

The above results were obtained under the assumption that all spirals possess the same dust-to-gas ratio throughout their disks at any given redshift. If the scatter in the dust content of different galaxies is large or if the dust distribution is patchy, then the quantitative impact of dust on the lensing statistics would be altered. Also, we have assumed

---

[5] See Myers and Williams & Schechter in Proceedings of the Workshop on Golden Lenses at Jodrell Bank (1997) at http://multivac.jb.man.ac.uk:8000/ceres/workshop1/proceedings.html.
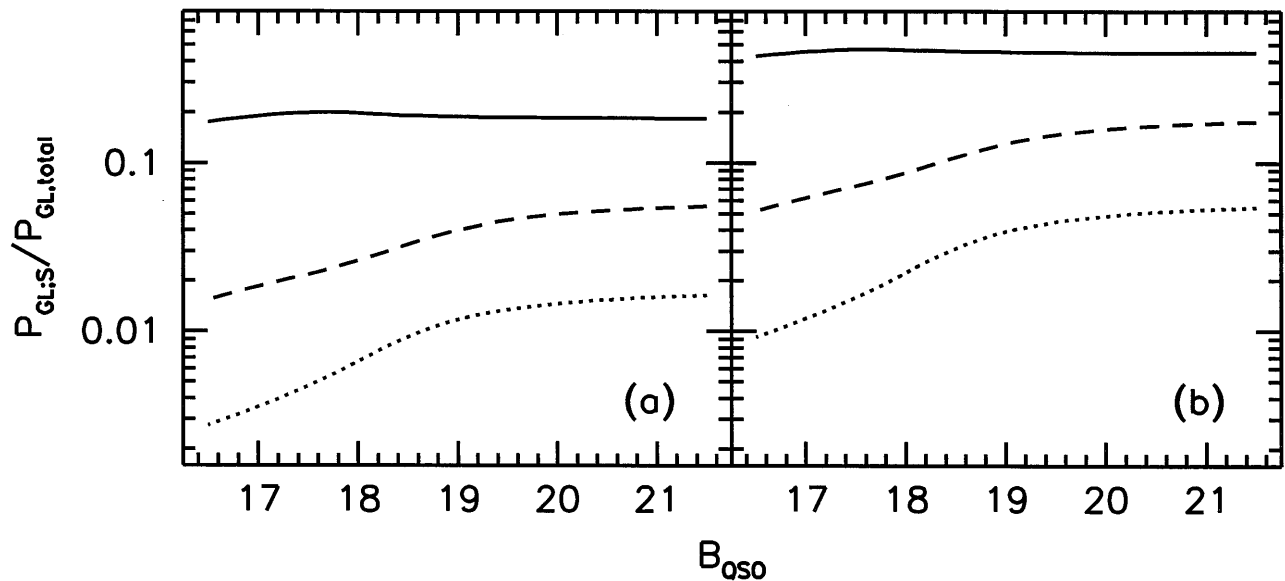
FIG. 12.—Fraction of the total multiple-imaging probability contributed by spiral galaxies. In (a) the early-type population is assumed to have constant comoving number density, and in (b) the number density of early-type galaxies evolves as a power law of redshift, so that $\frac{2}{3}$ of the early-type galaxies are in the form of spiral building blocks at $z = 1$. The three curves per panel are for spirals without dust (solid line), with nonevolving dust (dotted line), and with evolving dust (dashed line). Apart from merging to early-type galaxies, any other evolution of the spiral population was ignored.

that the scale heights of dust and gas are the same and that they are constant across the disk radius. On physical grounds, one would expect the scale heights of dust and gas to increase with radius, because their sound speed (which is set by the balance between cooling and heating) should not vary much with radius. In addition, if spiral disks at $z \lesssim 1$ are less massive than our *maximal disk* model assumes (see, e.g., Courteau & Rix 1998), then the lensing cross section of the disk and its related extinction signature would be reduced. Future studies should investigate these com-

plications by allowing submaximal disks, a range of scale heights, and possibly also patchy distributions for the gas and dust.

REFERENCES

Bahcall, J. N., & Peebles, P. J. E. 1969, ApJ, 156, L7
Bardeen, J. M., Bond, J. R., Kaiser, N., & Szalay, A. S. 1986, ApJ, 304, 15
Bartelmann, M., Huss, A., Colberg, J. M., Jenkins, A. R., & Pearce, F. R. 1998, A&A, 330, 1
Bartelmann, M., & Loeb, A. 1996, ApJ, 457, 529
Bothun, G., Impey, C., & McGaugh, S. 1997, PASP, 109, 745
Broeils, A. H., & van Woerden, H. 1994, A&AS, 107, 129
Browne, I. W. A., et al. 1997, in Observational Cosmology with the New Radio Surveys, ed. M. Bremer, N. Jackson, & I. Perez-Fournon (Dordrecht: Kluwer), 305
Corbett, E. A., Browne, I. W. A., Wilkinson, P. N., & Patnaik, A. R. 1996, in IAU Symp. 173, Astrophysical Applications of Gravitational Lensing, ed. C. S. Kochanek & J. N. Hewitt (Boston: Kluwer), 37
Courteau, S., & Rix, H.-W. 1998, ApJ, submitted (astro-ph/9707290)
Draine, B. T., & Lee, H. M. 1984, ApJ, 285, 89
Eke, V. R., Cole, S., & Frenk, C. S. 1996, MNRAS, 282, 263
Ellis, R. 1997, ARA&A, 35, 389
Faber, S., & Jackson, R. 1976, ApJ, 204, 668
Falco, E. E., Kochanek, C. S., & Muñoz, J. A. 1998, ApJ, 494, 47
Fall, S. M., & Efstathiou, G. 1980, MNRAS, 193, 189
Fall, S. M., & Pei, Y. C. 1993, ApJ, 402, 479
Fassnacht, C. D., & Cohen, J. G. 1998, AJ, 115, 377
Fassnacht, C. D., Womble, D. S., Neugebauer, G., Browne, I. W. A., Readhead, A. C. S., Matthews, K., & Pearson, T. J. 1996, ApJ, 460, L103
Freeman, K. C. 1970, ApJ, 160, 811
Fukugita, M., & Turner, E. L. 1991, MNRAS, 253, 99
Grundahl, F., & Hjorth, J. 1995, MNRAS, 275, L67
Holmberg, E. B. 1975, in Stars and Stellar Systems, Vol. 9, Galaxies and the Universe, ed. A. Sandage, M. Sandage, & J. Kristian (Chicago: Univ. Chicago Press), 151
Jackson, N., Nair, S., & Browne, I. 1997, in Observational Cosmology with the New Radio Surveys, ed. M. Bremer, N. Jackson, & I. Perez-Fournon (Dordrecht: Kluwer), 315
Jaunsen, A. O., & Hjorth, J. 1997, A&A, 317, L39
Kauffmann, G., Charlot, S., & White, S. D. M. 1996, MNRAS, 283, L117
Keeton, C. R., & Kochanek, C. S. 1998, ApJ, 495, 157

Knapp, G. R. 1987, PASP, 99, 1134
Kochanek, C. S. 1993, ApJ, 417, 438
———. 1996, ApJ, 466, 638
Koopmans, L. V. E., de Bruyn, A. G., & Jackson, N. 1998, MNRAS, 295, 534
Kulkarni, S. R., & Heiles, C. 1987, in Interstellar Processes, ed. H. Thronson & D. Hollenbach (Dordrecht: Reidel), 87
Kylafis, N. D., & Bahcall, J. N. 1986, ApJ, 317, 637
Lanzetta, K. M., Wolfe, A. M., Turnshek, D. A., Lu, L., McMahon, R. G., & Hazard, C. 1991, ApJS, 77, 1
Lauberts, A., & Valentijn, E. A. 1989, The Surface Photometry Catalogue of the ESO-Uppsala Galaxies (Munich: ESO)
Loeb, A. 1997, Proc. 1996 Texas Symposium, Chicago, in press (astro-ph/9701100)
Madau, P. 1997, in STScI Symp. Ser., The Hubble Deep Field, ed. M. Livio, S. M. Fall, & P. Madau, in press (astro-ph/9709147)
Malhotra, S., Rhoads, J., & Turner, E. 1997, MNRAS, 288, 138
Maller, A. H., Flores, R. A., & Primack, J. R. 1997, ApJ, 486, 681
Mao, S., & Kochanek, C. S. 1994, MNRAS, 268, 569
Marzke, R. O., Geller, M. J., Huchra, J. P., & Corwin, H. G., Jr. 1994, AJ, 108, 437
Menten, K. M., & Reid, M. J. 1996, ApJ, 465, L99
Mestel, L. 1963, MNRAS, 126, 553
Mo, H. J., Mao, S., & White, S. 1997, MNRAS, 295, 319
Myers, S. T., et al. 1995, ApJ, 447, L5
Navarro, J. F., Frenk, C. S., & White, S. D. M. 1995, MNRAS, 275, 56
O'Dea, C. P., Baum, S. A., Stanghellini, C., Dey, A., van Breugel, W., Deustua, S., & Smith, E. P. 1992, AJ, 104, 1320
Peacock, J. A., & Dodds, S. J. 1994, MNRAS, 267, 1020
Pei, Y. C. 1995, ApJ, 438, 623
Pei, Y. C., Fall, S. M., & Bechtold, J. 1991, ApJ, 378, 6
Perna, R., Loeb, A., & Bartelmann, M. 1996, ApJ, 488, 550
Peterson, B. M., Strom, S. E., & Strom, K. M. 1979, AJ, 84, 735
Press, W. H., & Schechter, P. L. 1974, ApJ, 181, 425
Ratra, B., Sugiyama, N., Banday, A. J., & Górski, K. 1997, ApJ, 481, 22
Rix, H.-W., Maoz, D., Turner, E. L., & Fukugita, M. 1994, ApJ, 435, 49

Schneider, P., Ehlers, J., & Falco, E. E. 1992, Gravitational Lenses (Heidelberg: Springer)

Smette, A., Claeskens, J., & Surdej, J. 1997, NewA, 2, 53

Storrie-Lombardi, L. J., McMahon, R. G., & Irwin, M. J. 1996, MNRAS, 283, L79

Strauss, M. A., & Willick, J. A. 1995, Phys. Rep., 261, 271

Tully, R. B., & Fisher, J. R. 1977, A&A, 54, 661

Tytler, D. 1987, ApJ, 321, 49

van der Kruit, P. C. 1987, A&A, 173, 59

Viana, P. T. P., & Liddle, A. R. 1996, MNRAS, 281, 323

Wang, Y., & Turner, E. 1997, MNRAS, 29, 863

White, S. D. M., Efstathiou, G., & Frenk, C. S. 1993, MNRAS, 262, 1023

Whittet, D. C. B. 1992, Dust in the Galactic Environment (Philadelphia: Hilger)

Wiklind, T., & Combes, F. 1995, A&A, 299, 382

Xilouris, E. M., Kylafis, N. D., Papamastorakis, J., Paleologou, E. V., & Haerendel, G. 1997, A&A, 325, 135